*Article*

# Investigation of the Surface Coating, Humidity Degradation, and Recovery of Perovskite Film Phase for Solar-Cell Applications

**Amal Bouich** [1,2,3,*]**, Julia Marí-Guaita** [1]**, Faisal Baig** [1,4]**, Yousaf Hameed Khattak** [1,4]**, Bernabé Marí Soucase** [1,*] **and Pablo Palacios** [2,3]

1 Escuela Técnica Superior de Ingeniería del Diseño, Universitat Politècnica de València, 46022 València, Spain
2 Instituto de Energía Solar, ETSI Telecomunicación, Universidad Politécnica de Madrid, Ciudad Universitaria, s/n, 28040 Madrid, Spain
3 Department Física Aplicada a las Ingenierías Aeronáutica y Naval, ETSI Aeronáutica y del Espacio, Universidad Politécnica de Madrid, Pz. Cardenal Cisneros, 3, 28040 Madrid, Spain
4 Electrical Engineering Department, Federal Urdu University of Arts, Sciences and Technology, Islamabad 44000, Pakistan
* Correspondence: bouich.amal@gmail.com (A.B.); bmari@fis.upv.es (B.M.S.)

**Abstract:** Presently, we inquire about the organic/inorganic cation effect on different properties based on structure, morphology, and steadiness in preparing a one-step solution of APbI$_3$ thin films, where A = MA, FA, Cs, using spin coating. This study was conducted to understand those properties well by incorporating device modeling using SCAPS-1D software and to upgrade their chemical composition. X-ray diffraction (XRD) was used to analyze the crystal structures. Atomic Force Microscopy (AFM) and Scanning Electron Microscopy (SEM) were conducted to characterize the surface morphology; photoluminescence, Transmission Electron Microscopy (TEM), and a UV–Visible spectrometer helped us to study the optical properties. The (110) plane is where we found the perovskite's crystalline structure. According to the XRD results and by changing the type of cation, we influence stabilization and the growth of the $APbI_3$ absorber layer. Hither, a homogenous, smooth-surfaced, pinhole-free perovskite film and large grain size are results from the cesium cation. For the different cations, the band gap's range, revealed by the optical analysis, is from 1.4 to 1.8 eV. Moreover, the stability of $CsPbI_3$ remains excellent for two weeks and in a ~60% humid environment. Based on the UV–Visible spectrometer and photoluminescence characterization, a numerical analysis for fabricated samples was also performed for stability analysis by modeling standard solar-cell structures $HTL/APbI_3/ETL$. Modeling findings are in good agreement with experimental results that $CsPbI_3$ is more stable, showing a loss % in PCE of 14.28%, which is smaller in comparison to $FAPbI_3$ (44.46%) and $MAPbI_3$ (20.24%).

**Keywords:** thin films; $APbI_3$; organic/inorganic perovskite; optical properties; stability; SCAPS-1D; numerical analysis

## 1. Introduction

The decline of fossil fuels and global warming are responsible for the global demand for renewable energy resources and the development of advanced technology for producing them. The use of natural resources permits the production of energy from renewable energy resources [1,2]. It is imperative that the scientific community expands to make use of these resources efficiently. Global challenges of generating energy from renewable resources can be met with the help of solar energy [3,4]. Substantial efforts are required to develop novel photovoltaic technologies that guarantee cost reduction with enhanced

efficiency. The research community has a rising interest in perovskite solar cells (PSCs) among other technologies because of the ease of the fabrication process and higher conversion efficiency [5–10].

The first PSC was reported in 2009 as having a power-conversion efficiency (PCE%) of 2.2% [11,12]. After extensive research, in 2011 researchers improved the efficiency by around 6.5% along with inadequate stability [13]. The conversion efficiency further improved to 9.7% in 2012 [14]. Researchers pay keen attention to PSCs because the PCE reached 15% in 2013 [15]. In 2014, Yalçin et al. presented PSC top efficiency of around 20% [16] and Devi et al. improves that PCE to 23.30% with 1.55 eV of bandgap in 2019 [17,18]. In the near future, the commercialization and stabilization of PSCs will increase greatly since 25.2% of efficient PSCs were recently verified and reported by KRICT and MIT. Results were also tested and verified by Newport PV Laboratory [19]. This is incredibly close to 26.7% efficient crystalline silicon solar cells [20,21]. The instant growth in the PSCs performance is the primary reason for the gigantic boost in the research, manufacturing, and development of PSCs. High absorption coefficient and long carrier diffusion length are also the cause for the further development of PSC technology [22,23].

Organic-inorganic halide perovskites are exceptionally fascinating absorber/active materials in thin-film technology due to their exceptional prominent device performance (solar cells and LEDs) and exceptional tunable optoelectronic properties [24–28]. Recently, a profound study has been made on hybrid perovskites $(APbX_3)$ due to their long carrier-diffusion length, high absorption, stability and carrier mobility, small effective hole/electron masses, and low exciting binding energies [29–34]. Consequently, the success of these synthesized compounds has been seen in manufacturing lasers [35,36] polarizers [37], diodes [38,39] photodetectors [40,41], and solar-cell [42,43] manufacturer technology.

Generally, the solar cells comprise the sandwiched configuration of having perovskite photoactive/absorbers type $ABX_3$, charge transport layers, and counter electrodes. Halide perovskite materials can be denoted by $ABX_3$; wherever A is an organic methylammonium $(CH_3NH_3^+ \text{ or } MA)$ and formamidinium $(NH_2CH = NH_2^+ \text{ or } FA)$ cesium $(Cs^+ \text{ or } Cs)$ ions, B can be an inorganic cation $(Sn_2^+ \text{ or } Pb_2^+)$, and X can be a halogen ion $(Cl^-, Br^- \text{ or } I^-)$ [44–46]. Amongst them, the extremely conventional promising active materials are methylammonium lead iodide $(MAPbI_3$, formamidinium lead iodide $(FAPbI_3)$, and cesium lead iodide $(CsPbI_3)$ [47–50]. To realize the efficiency determination of PSCs, we should base the study on the interface of perovskite layers, the transportation process, and the charge extraction. Consequently, we can say that there is a parallel between each path of the crystal quality and the system's efficiency, and at the interface, non-radiative recombination reduces. The development of the first leads to the enhancement of the other. In our work, the investigation primarily focuses on the cation lead iodide's stability $APbI_3$ (where A can be Cs, MA, and FA), and the wide absorption range of the PSC phase. At UV–Vis wavelengths and to optimize photon absorption, the present studies concentrate on halide exchange to modify the bandgap. This work is divided into three main categories.

We describe a new method for altering the bandgap of halide perovskites by elaborating on cation materials. We have synthesized organic-inorganic lead halide perovskites $(APbI_3$, where A = mixed monovalent cation systems MA/Cs/FA), using the spin-coating process; this method is a low-cost technique for thin-film material deposition. After the successful fabrication of samples, we performed different characterization studies on as-deposited samples. Then we performed a detailed study of the degradation and recovery of the perovskite phase of deposited samples by studying their optical absorption and crystal structures along with the physical appearance of samples. Lastly, we performed a numerical analysis study of these materials to provide insight into physics for as-deposited, degraded, and recovered samples by simulating standard solar-cell structure $HTL/APbI_3/ETL$ in SCAPS-1D, where $APbI_3$ is replaced with $MAPbI_3$, $FAPbI_3$ and $CsPbI_3$.

## 2. Thin-Film Manufacture

### 2.1. Experimental Procedure

Lead (II) iodide ($PbI_2$), methylammonium iodide ($MAI$), cesium iodide ($CsI$), formidinium iodide ($FAI$) purchased from sigma Aldrich, N,N-dimethylformamide anhydrous ($DMF$), and dimethyl sulfoxide ($DMSO$) from Thermo Scientific, the antisolvent chlorobenzene from Sigma-Aldrich, were used as precursor materials to fabricate the perovskite thin-film solutions. Then the prepared solution of $APbI_3$, where ($A = Cs, MA, FA$), was spin-coated for 20 s at 2000 rpm on the $FTO$ substrate. The deposition procedure is shown in Figure 1, where on top we displayed steps to deposit perovskite samples via the spin-coating method and at bottom of Figure 1 we displayed the as-deposited samples along with precursor solutions for perovskite materials.
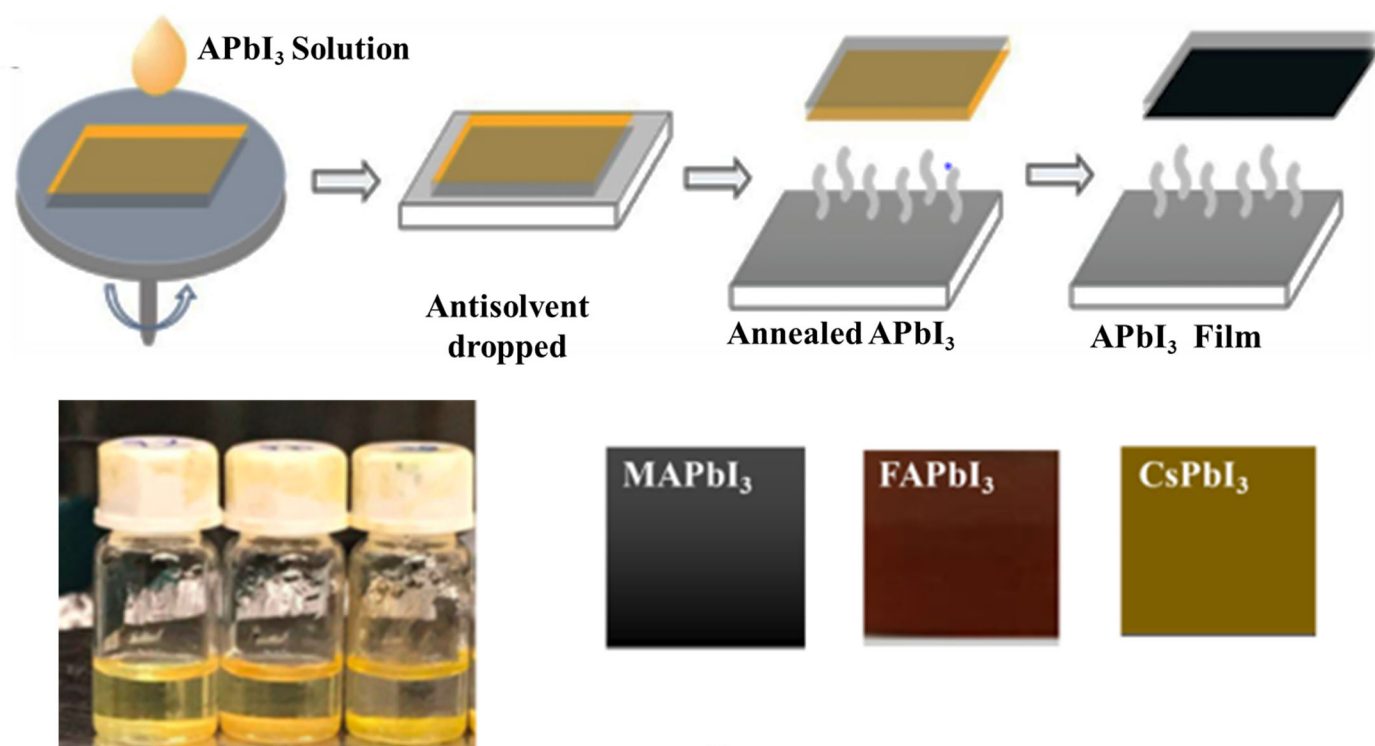


**Figure 1.** $APbI_3$ where $A = MA/FA/Cs$ films were manufactured with a low-cost technique.

### 2.2. Film Characterization

Different characterization techniques were used to evaluate the as-deposited samples of perovskite materials. The perovskite thin film's crystal-structure analysis was performed by $XRD$ RIGAKU Ultima IV diffractometer, $SEM$ (Scanning Electron Microscopy) was performed to find the morphology of the deposited sample at different magnification levels, $AFM$ (Atomic Force Microscopy) was performed to characterize the deposited film's topography analysis, and $TEM$ (Transmission Electron Microscopy) was also performed to authenticate the formation of perovskite structures. The absorption was calculated using a UV-Visible wavelength range of 300 to 850 nm, and photoluminescence (PL) was performed by He-Cd laser.

## 3. Results and Discussion

The impact of changing cation A on the thin films' microstructure was explored by XRD Figure 2, where we can see the locations and the plans of diffractions peaks: 14.0 (110), 24.0 (202), 28.0 (220), 32.0 (222), 37.5 (400), and 52.0 (303). These crystal structures are fundamentally very similar; growth was shown at the peak at 2θ = 14°, which corresponds to $MAPbI_3$ shown in Figure 2a and $FAPbI_3$ (110) as (hkl) shown in Figure 2c. The

orange phase is also for the (110) peak of $CsPbI_3$ shown in Figure 2b, which is the most prominent peak among the three compounds. However, a continuous displacement between the crystal structures is observed. Substantially, there is a highly crystalline phase, especially when there is an overly lattice strain. This remark shows the ability to substitute readily for the cations (MA, FA, and Cs) across the lattice without harming the crystal structure. The $MAPbI_3$ structure to be studied is correlated with the same diffraction peaks. Furthermore, the height (110) intensity is enhanced for the $CsPbI_3$ film.

The XRD pattern uncovered the enhanced crystallite orientation alongside the (110) plane. As a result of the solvent treatment, a tetragonal lattice has factored a = b = 8.919 Å and c = 11.920 Å, which corresponds to the space group I4/mcm, and the film of perovskite $MAPbI_3$ crystallizes. However, when $CsPbI_3$ was heat-treated for 10 min at 180 °C, these diffraction peaks can be allocated to cubic phase (a = 6.18 Å, space group Pm3m), and up to 180 °C in temperature, $a - CsPbI_3$ was formed as in the crystalline phases. These results indicated the efficiency of the synthesis of $CsPbI_3$ in the standard conditions, and the crystallization trend of perovskite was proper during synthesis [51].
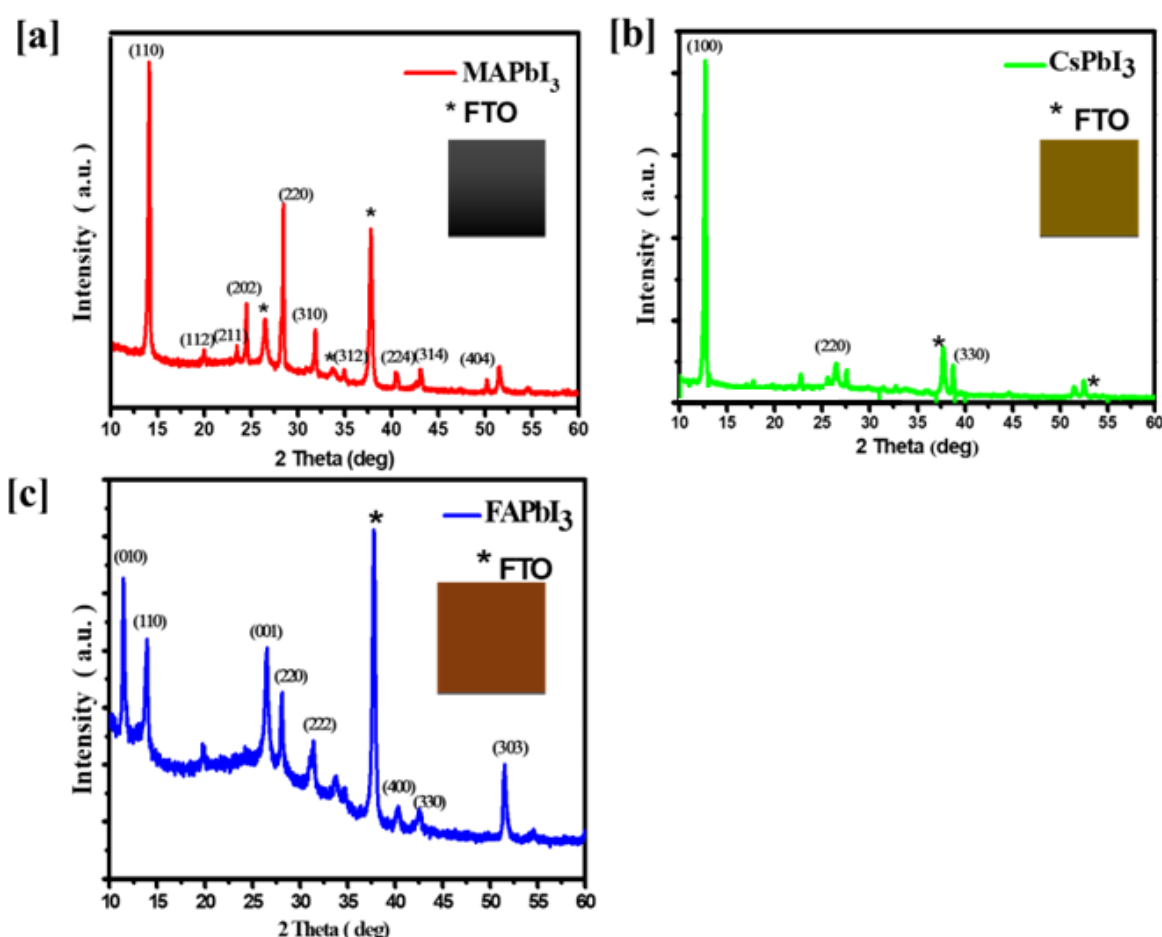


**Figure 2.** XRD patterns of (**a**) $MAPbI_3$, (**b**) $CsPbI_3$, and (**c**) $FAPbI_3$ thin films.

The roughness and surface morphology changes with different cations in the perovskite thin films. The parameters are revealed in Table 1. Effective lattice strain has been calculated to know about the deformations of the grains in the surface of the film. To acquire the effective lattice strain (ε) Equation (1) was used [52].

$$\beta \cos(\theta) = \frac{k\lambda}{D} + 4\varepsilon \sin(\theta) \tag{1}$$

where $\lambda$ is the wavelength of the X-ray, $\beta$ is the full width half maximum (FWHM), k is a constant (0.94), and $\theta$ is the Bragg angle. Equation (2) was applied to determine the dislocation density of the crystal.

$$\delta = \frac{1}{D^2} \tag{2}$$

**Table 1.** $APbI_3$ thin films XRD parameters.

| Sample ID | Lattice Strain ($\varepsilon \times 10^{-3}$) | Grain Size (nm) | Dislocation Density (nm$^{-1}$) | Roughness (nm) |
|---|---|---|---|---|
| $MAPbI_3$ | 9.05 | 331 | $0.91 \times 10^{-5}$ | 145 |
| $CsPbI_3$ | 8.71 | 345 | $0.84 \times 10^{-5}$ | 420 |
| $FAPbI_3$ | 8.13 | 283 | $1.13 \times 10^{-5}$ | 231 |

Scanning electron micrography was the technique used to investigate the morphology of the films at many points in Figure 3. At first, large crystallites and a few large pinholes are the morphology of the $MAPbI_3$. As the change in the cation of MA by FA and Cs, there is a formation of a few crystals distributed randomly on the surface of $FAPbI_3$. The appearance of structures in destroyed shapes coincides with peaks corresponding to the yellow phase in XRD; this is the preferred crystal habit of the yellow $FAPbI_3$. Pinholes that are several nanometers were observed on the surface of $MAPbI_3$ annealed at 120 °C; in the case of $CsPbI_3$ perovskite, there are not plenty of pinholes in the thin film annealed at 180 °C. When the heat-treatment temperature was raised to 200 °C, it was clear that $CsPbI_3$ started to crystallize, and the grains were more regular. The effect could be explained by the $MAPbI_3$ perovskite becoming unstable under the same conditions, serving as a degraded model after a short amount of time. At the same time, the control film shows signs of $\delta - CsPbI_3$ at a temperature of 180 °C. To explain the better absorbance, there is a formation with a thicker and regular thickness of intimate contact with the underlying layer, which is compact and smooth with better-packed grains, which contained the resultant $CsPbI_3$ film annealed at 200 °C.
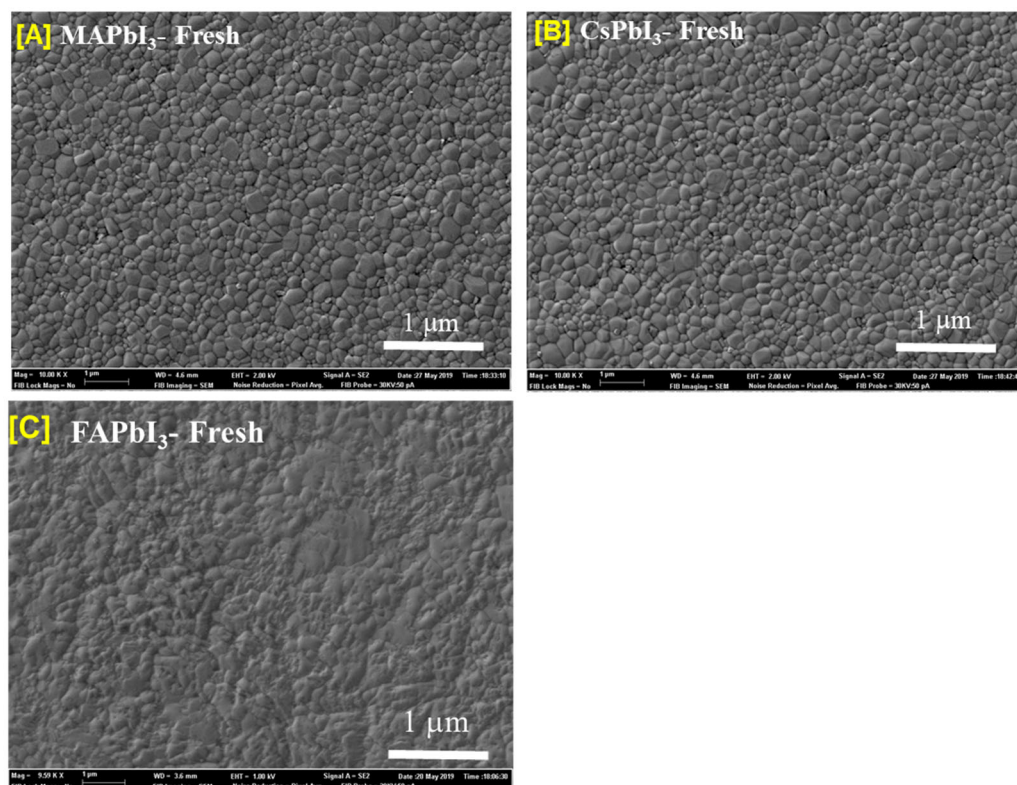


**Figure 3.** (SEM) images of the surface morphology of (**A**) $MAPbI_3$, (**B**) $CsPbI_3$, and (**C**) $FAPbI_3$.

The surface morphology of samples is an important parameter for perovskite solar cells as they can directly affect the quantum efficiency (QE) of perovskite materials. To analyze the surface roughness of deposited perovskite material, AFM study was conducted, as the roughness parameter often results in many holes which create resistance and, consequently, decrease the charge mobility of carriers. Figure 4 shows the results for the surface roughness of perovskite materials, and from Figure 4 it is clear that surface height and valley point in MA- and Cs-doped perovskite are lesser than that of FA-doped perovskite material [53].
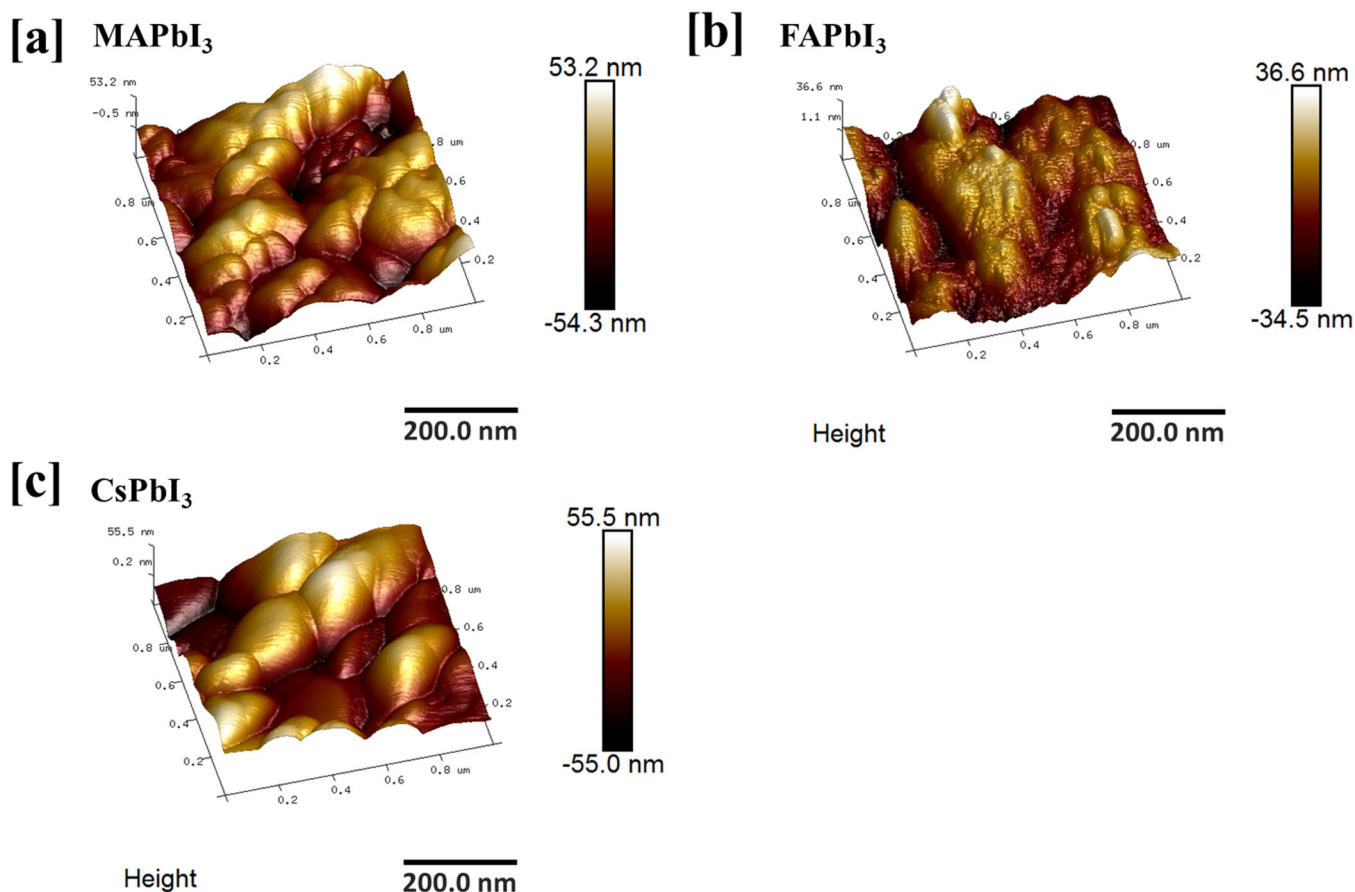


**Figure 4.** The topographic property of (**a**) $MAPbI_3$, (**b**) $FAPbI_3$, (**c**) $CsPbI_3$ films.

Figure 5 indicates the TEM characterization of polycrystalline $MAPbI_3$ thin films. Further, 0.28 nm is the lattice fringe equivalent to (110) or (220) of the $MAPbI_3$ phase. $FAPbI_3$ thin films: 0.64 nm is the lattice fringe equivalent to (110) of the $FAPbI_3$ phase. $CsPbI_3$ thin films: 0.36 nm is the lattice fringe equivalent to (100) of the $CsPbI_3$ phase.
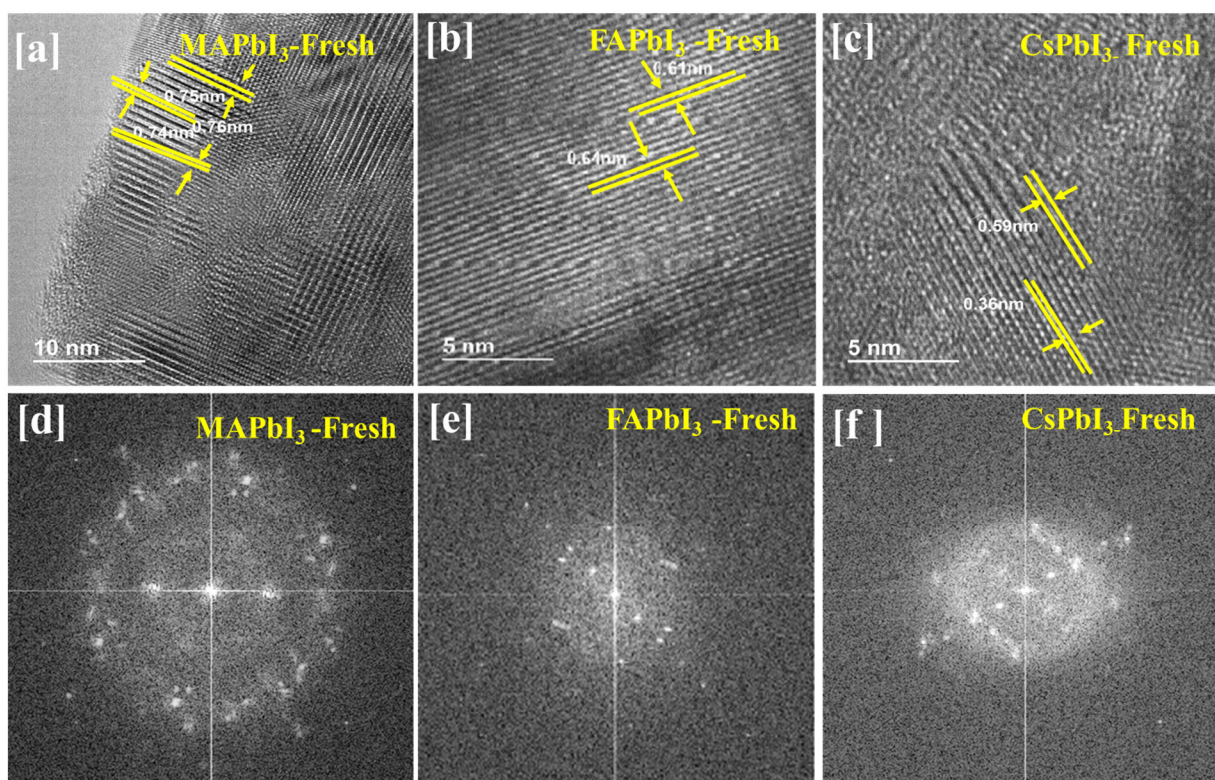
**Figure 5.** TEM images of the surface morphology of (**a**–**d**) $MAPbI_3$, (**b**–**e**) $FAPbI_3$, and (**c**–**f**) $CsPbI_3$.

The PL measurements were canned at the ambient temperature as shown in Figure 6b. The PL peak intensity between 700–850 nm previously mentioned progressively increases with the $CsPbI_3$ film. However, by changing the cation A (FA) by MA and Cs, the PL intensities vary. A suggestion is that $CsPbI_3$ thin film is the optimal level at which it can better ambush, owing to the improvement of crystallinity and surface passivation, the absorption shift.

The corresponding UV–Vis spectra of $MAPbI_3$, $FAPbI_3$, and $CsPbI_3$ were recorded [300 nm–1000 nm] (Figure 6a). Different cations shift the absorption edge to a high wavelength, reducing the perovskite films' defect density and increasing their crystallization quality. Furthermore, the optical bandgap is in good agreement.
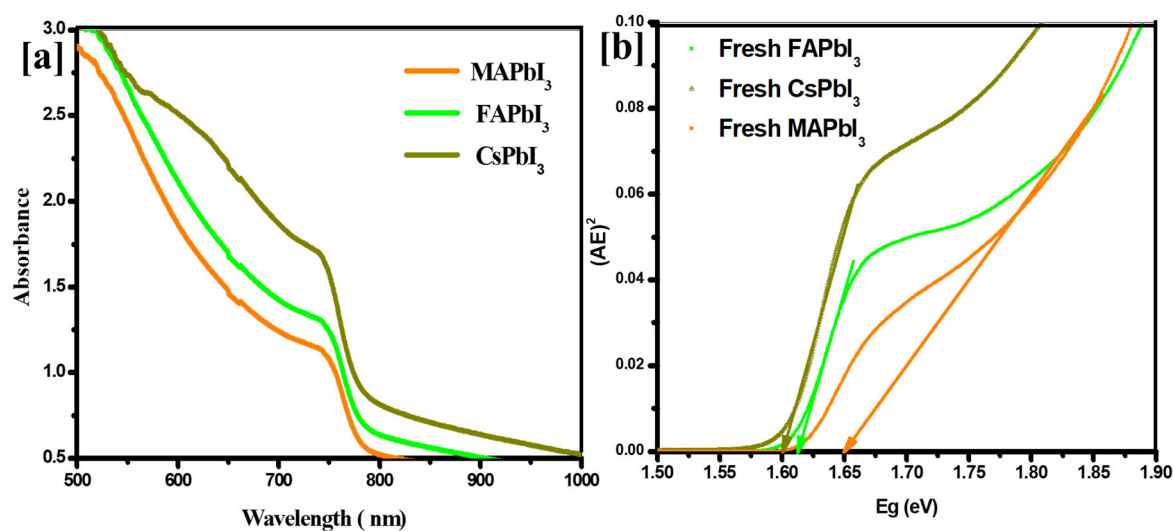


**Figure 6.** (**a**) Absorption and (**b**) Bandgap energy for of $MAPbI_3$, $FAPbI_3$, and $CsPbI_3$.

The optical bandgap is in good agreement with the literature (Table 2), where it reduces drastically until an optimal level as shown in Figure 7. The intercalation of the cesium as a cation regulates the optical properties of $CsPbI_3$ semiconductor materials for photovoltaic devices [54].

**Table 2.** $APbI_3$ thin films' optical properties.

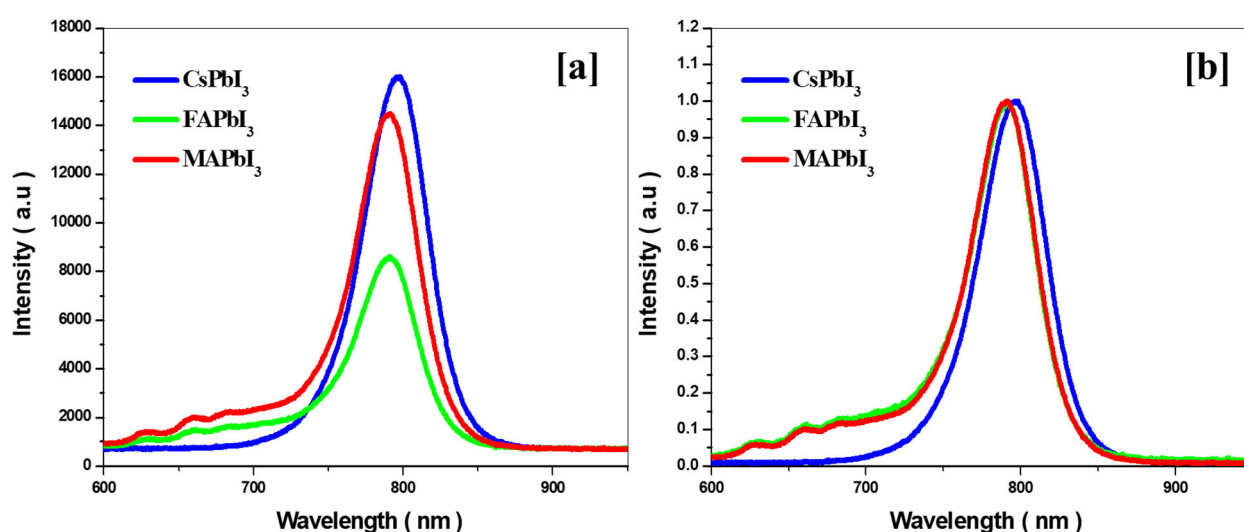| Sample ID | Optical Band Gap by Absorption | | Emission PL Peak | | Stokes Shift |
|---|---|---|---|---|---|
| | $\lambda c$ (nm) | $Eg$ (eV) | $\lambda$ (nm) | $Eg$ (eV) | (meV) |
| $MAPbI_3$ | 719 | 1.55 | 760 | 1.40 | 150 |
| $FAPbI_3$ | 795 | 1.50 | 770 | 1.35 | 150 |
| $CsPbI_3$ | 752 | 1.53 | 768 | 1.36 | 180 |



**Figure 7.** (**a**) Photoluminescence (PL) (**b**) normalized PL for $MAPbI_3$, $CsPbI_3$, and $FAPbI_3$ thin films.

## 4. Degradation Study

The serious problems are the stability issues for the commercialization of perovskite solar cells. The halide perovskite components are related through weak interactions such as ionic and hydrogen bonding. The decomposition of organic species and the ion migration happen quickly in perovskite solar cells under moisture penetration as shown in Figures 8 and 9 [55]. In this part, we discuss the stability from the viewpoint of cation exchange, $CsPbI_3$, $MAPbI_3$, and $FAPbI_3$ stabilization, and the best solution for reducing efficiency leakage. Figure 8 shows pictures of samples that were put in 60% humidity under dark conditions, and from Figure 8 it is clear that $MAPbI_3$ and $FAPbI_3$ have gone through degradation while $CsPbI_3$ shows resilience against humidity. A few pinholes were observed in samples just by visually inspecting the surface of the samples. The crystallography of the same samples was also analyzed by performing XRD of these samples.
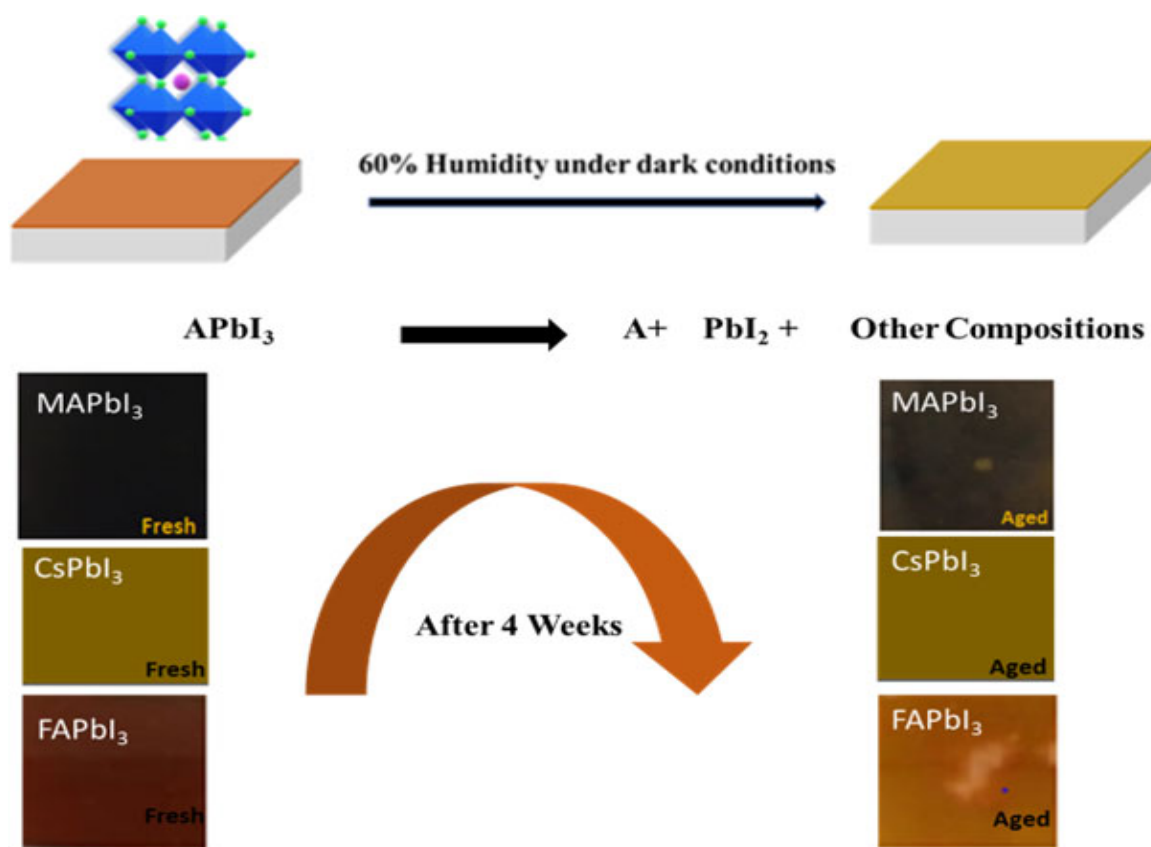
**Figure 8.** Degradation mechanism of $APbI_3$ in the air at 60% humidity and under dark conditions.
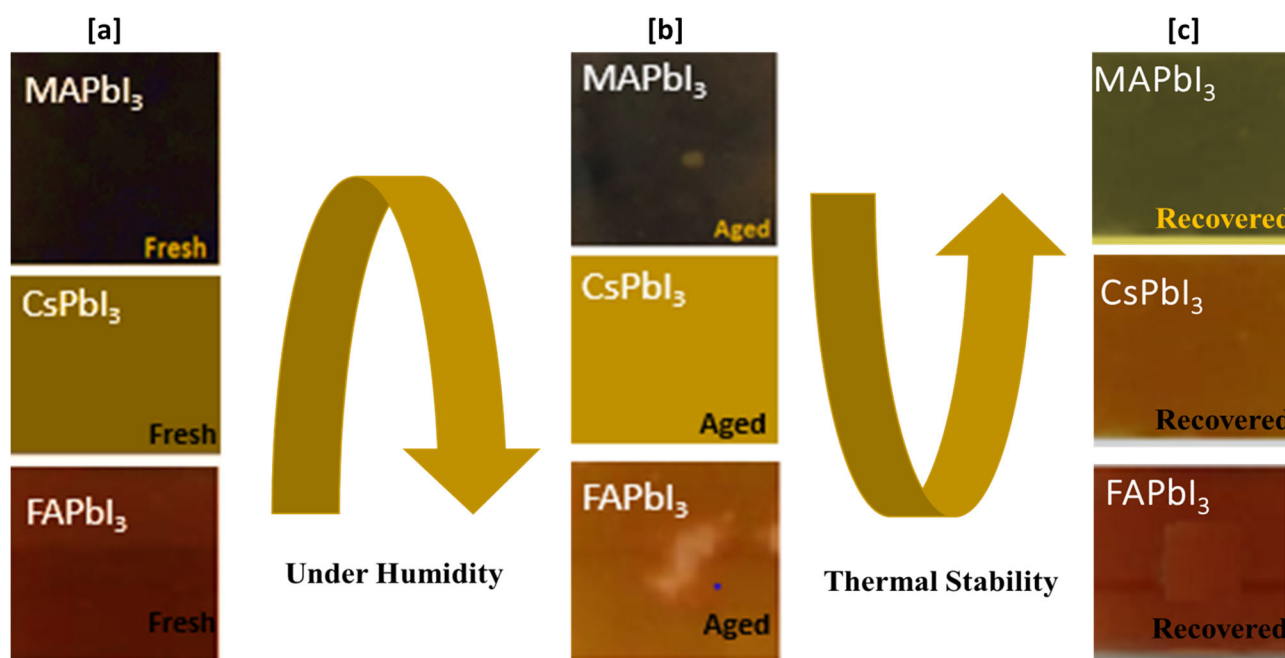


**Figure 9.** Recovery mechanism of $APbI_3$ in the air at 60% humidity and under dark conditions. (**a**) As deposited samples (**b**) Degradation of samples (**c**) Recovery after thermal treatment of samples

Figure 10 shows the XRD patterns of fresh $MAPbI_3$, $FAPbI_3$, and $CsPbI_3$ thin films, aged for four weeks in the air at 60% humidity under dark conditions and recovered with thermal treatment under temperature 100 C. Although no technique is generally used to measure the stability of perovskite thin films, a simple procedure was developed to

analyze them. By comparing the values of the intensities, this method was developed to detect the most stable thin film. Relative to fresh spectra, essential changes do not happen in ranges; for example, in the appearance of new peaks, a percentage decrease in intensity appears to relate with stability since the number of perovskite diffraction planes is proportional to the total power. This phenomenon explains that the new the peaks that appear on older films correspond to new phases and demonstrate the partial degradation of the $MAPbI_3$, $FAPbI_3$, and $CsPbI_3$ thin films. The recovered $FAPbI_3$ and $CsPbI_3$ samples showed significantly increased stability by thermal treatment due to the hysteretic effect of these materials related to phase transition. Remarkably, the intensity of the recovered pieces is higher than the aged $CsPbI_3$ and $FAPbI_3$ prepared. On the other hand, the $MAPbI_3$ film showed low stability compared to the perovskite based on cesium, see Figure 10. This study suggests that $CsPbI_3$ improves crystal quality and has high stability. However, we can see the appearance of the non-perovskite Ɣ phase for the $FAPbI_3$ film in the spectrum in Figure 10b, showing that parts of the structure had deteriorated in new phases; thus, we can announce that this study proves that $CsPbI_3$ is the most efficient in these conditions. The absorption results confirm this conclusion where the aged $CsPbI_3$ and $FAPbI_3$ and $MAPbI_3$ samples show a dramatic decrease compared to the fresh and recovered samples, and these results are plotted in Figure 11.
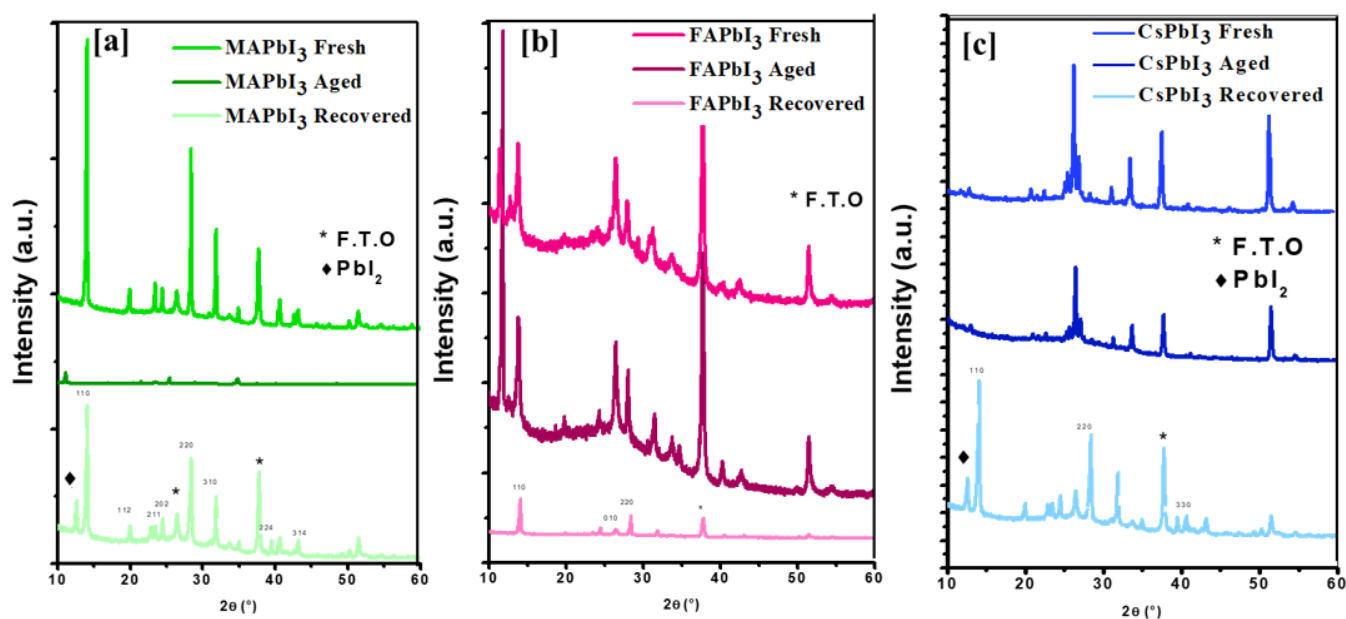


**Figure 10.** XRD characterization of $APbI_3$ samples in the air at 60% humidity and under dark conditions; (**a**) $MAPbI_3$, (**b**) $FAPbI_3$, (**c**) $CsPbI_3$.
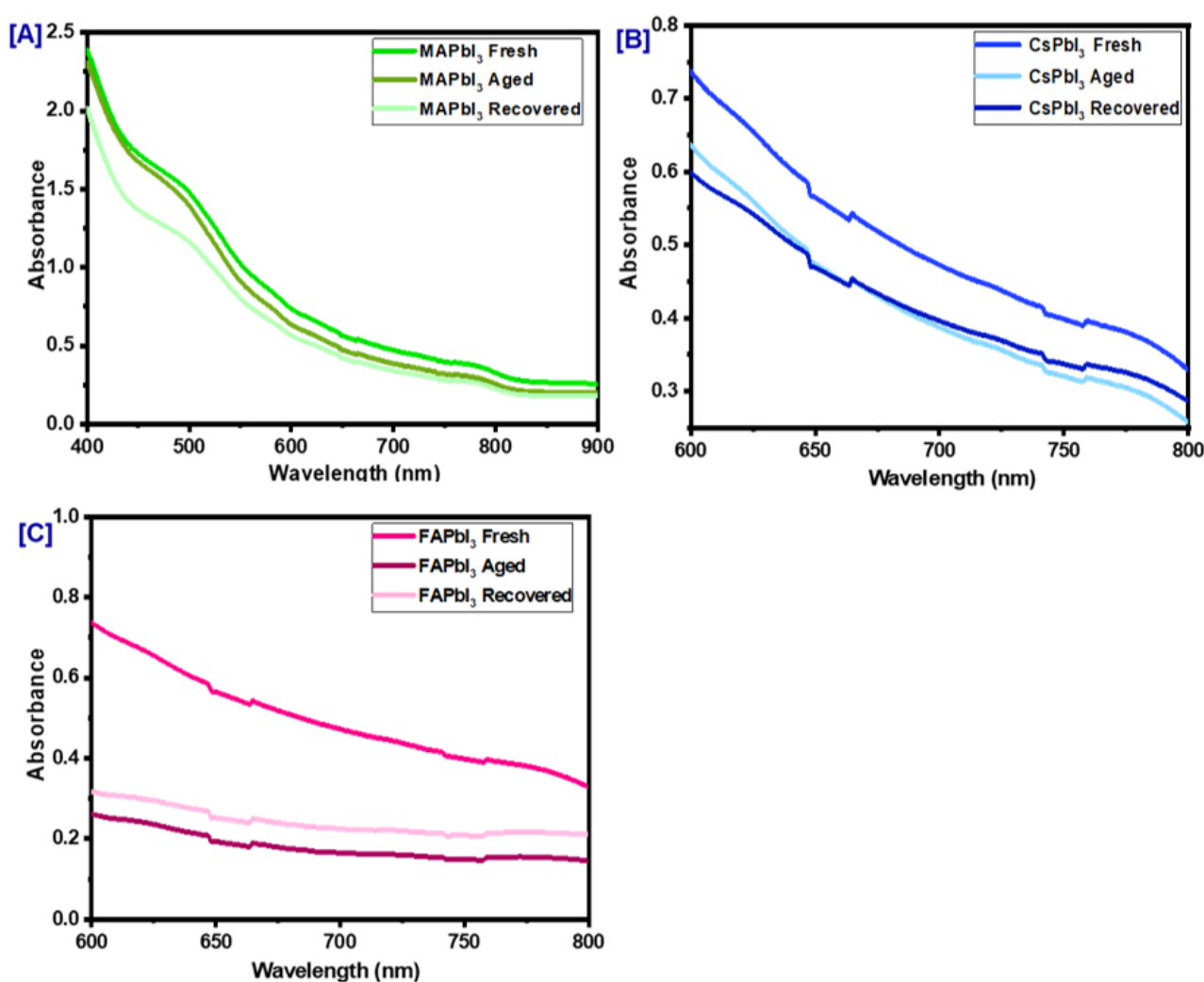
**Figure 11.** Optical absorption of $APbI_3$ samples in the air at 60% humidity and under dark conditions; (**A**) $MAPbI_3$, (**B**) $CsPbI_3$, (**C**) $FAPbI_3$.

## 5. Film Recovering

From the photographs $APbI_3$, as shown in Figures 8 and 9, the color changes from a deep color to a clear color due to the dissociation or phase transition of perovskite. The same process was also analyzed with the subject to SEM studies by analyzing the surfaces of the deposited, degraded, and thermally treated samples. From Figure 12, a pinhole and change in surface morphology are apparent for pure aged FA and MA samples compared to fresh ones, but we can note that for $Cs$ samples that show good stability and are well recovered by thermal treatment, the surface shows fewer pinholes. This is in agreement with the results of the absorption spectra (plotted in Figure 11) and visual inspection in Figure 9, which confirms the stability; here, we can offer the route to enhance the stability of $APbI_3$. We confirm that the incorporation of ($Cs$) enhances the stabilization of perovskite and our results are in good agreement with the literature [56].
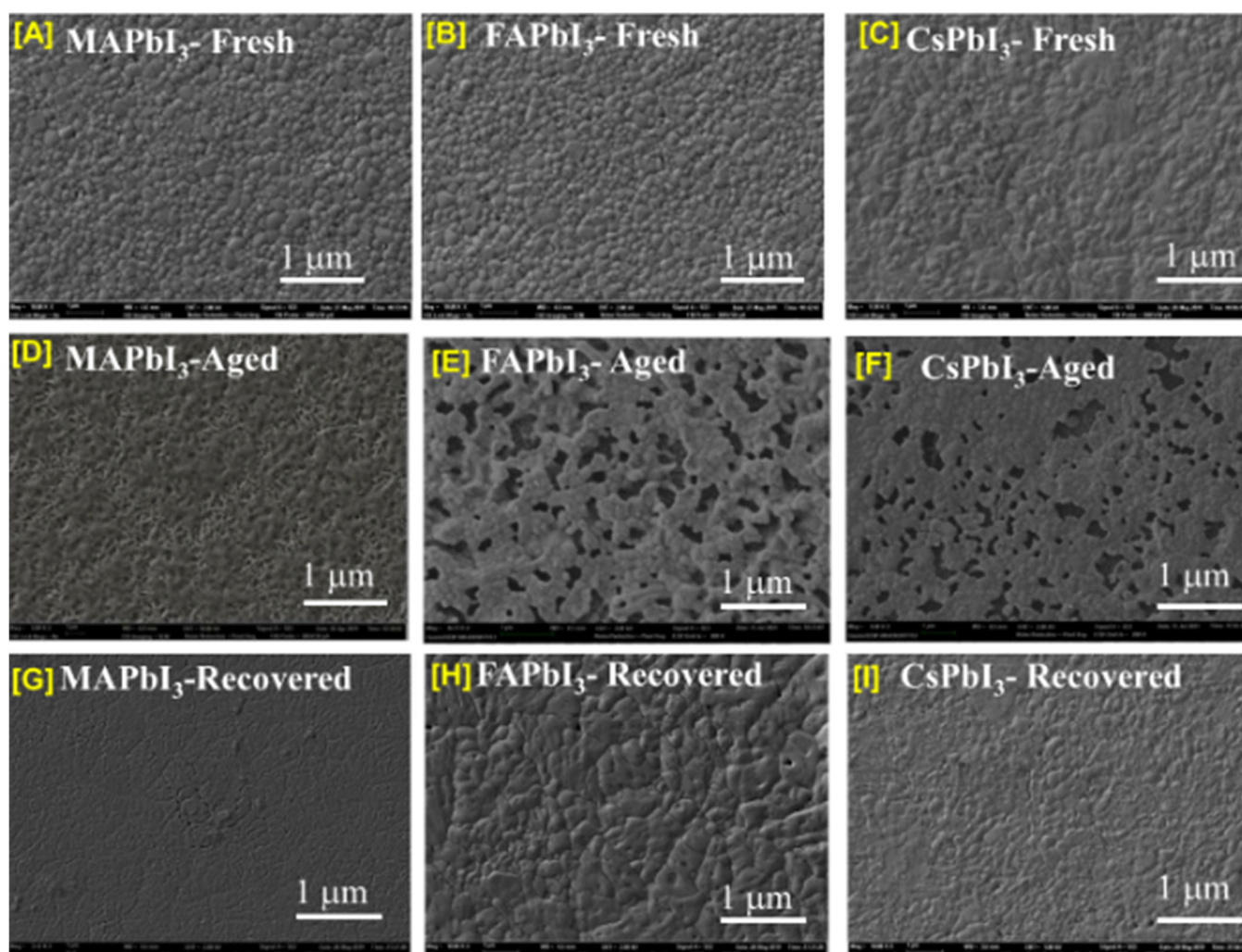
**Figure 12.** Fresh, degraded and recovered samples of $APbI_3$ in the air at 60% humidity and under dark conditions: (**A,D,G**) $MAPbI_3$ (**B,E,H**) $FAPbI_3$ (**C,F,I**) $CsPbI_3$.

## 6. Numerical Analysis

Device modeling for as-deposited, aged, and recovered samples was performed in SCAPS, and the simulation parameters that were used for the given device structure $HTL/APbI_3/ETL$ are given in Tables 3–5.

SCAPS-1D is a solar-cell capacitance software that is used to calculate the functional parameters of the solar cell, such as short circuit current ($Jsc$), open-circuit voltage ($Voc$), Fill factor (FF%), and power-conversion efficiency (PCE%), based on the input parameters given in Tables 3 and 4 and the absorption profile for each layer [57,58]. SACPS-1D, over years, has proven to be a significant tool for understanding the physics of solar cells and it has been comprehensively used for perovskite solar cells [59–64]. SCAPS also calculates AC quantities, electron/hole densities, quantum efficiencies (QE%)/spectral response, total recombination currents, energy band diagrams, and current density vs voltage characteristics [65–73] It is based on drift-diffusion differential equations and Poisson's carrier (electron/hole transport) continuity equations [63,64].

**Table 3.** Simulated-device physical input parameters [58,70–73].

| Parameters | $Spiro-OMeTAD$ (HTL) | $MAPbI_3$ (Absorber) | $FAPbI_3$ (Absorber) | $CsPbI_3$ (Absorber) | $TiO_2$ (ETL) |
|---|---|---|---|---|---|
| $W$ (μm) | 0.6 | 0.4 | 0.4 | 0.4 | 0.1 |
| $E_g$ (eV) | 3 | 1.55 | 1.5 | 1.53 | 3.2 |
| $\chi$ (eV) | 2.45 | 3.9 | 4.0 | 3.88 | 4 |
| $\epsilon_r$ | 3 | 10 | 6.6 | 6 | 9 |
| $N_c$(cm$^{-3}$) | $2.2 \times 10^{18}$ | $2.8 \times 10^{18}$ | $1.2 \times 10^{19}$ | $1.1 \times 10^{20}$ | $1 \times 10^{19}$ |
| $N_v$ (cm$^{-3}$) | $1.1 \times 10^{19}$ | $3.9 \times 10^{18}$ | $2.9 \times 10^{18}$ | $8 \times 10^{19}$ | $1 \times 10^{19}$ |
| $n, p$ (cm$^{-3}$) | $1 \times 10^{15}$ | $1 \times 10^{14}$ | $1 \times 10^{14}$ | $1 \times 10^{14}$ | $1 \times 10^{16}$ |
| $\mu_e$ (cm$^2$/Vs) | 0.0002 | 11.8 | 2.7 | 16 | 20 |
| $\mu_p$ (cm$^2$/Vs) | 0.0002 | 11.8 | 2.8 | 16 | 10 |

**Table 4.** Defects in layers and interfaces.

| Defect Properties | $Spiro-OMeTAD$ | Absorber | $Spiro-OMeTAD/$ Absorber |
|---|---|---|---|
| $N_t$ | $1 \times 10^{16}$ (cm$^{-3}$) | $3 \times 10^{14}$ (cm$^{-3}$) | $1 \times 10^{14}$ (cm$^{-2}$) |
| $E$ (eV) | 0.6 | 0.6 | 0.32 |
| $\delta_e$(cm$^2$) | $1 \times 10^{-14}$ | $1 \times 10^{-14}$ | $1 \times 10^{-16}$ |
| $\delta_h$(cm$^2$) | $1 \times 10^{-14}$ | $1 \times 10^{-14}$ | $1 \times 10^{-16}$ |

$N_t$: Total density  $E$: Energy level  $\delta_h, \delta_e$: Holes and electrons capture cross section area

**Table 5.** Percentage loss in different fabricated solar cells PCE; $MAPbI_3$, $FAPbI_3$, and $CsPbI_3$.

| Samples | Fabricated Samples PCE [%] | Degraded Samples PCE [%] | Loss Percentage in PCE [%] |
|---|---|---|---|
| $MAPbI_3$ | 22.93 | 18.29 | 20.24 |
| $FAPbI_3$ | 20.74 | 11.52 | 44.46 |
| $CsPbI_3$ | 19.12 | 16.39 | 14.28 |

The $HTL/APbI_3/ETL$ desired structures were simulated in SCAPS-1D software; in this, $Spiro-OMeTAD$ was used as HTL, $APbI_3$ is a perovskite absorber layer with A replacing $(MA, FA, Cs)$ and $TiO_2$ is used as ETL layer. The physical parameters for all structures remained constant, as shown in Tables 3 and 4, and the only things that we changed in the absorption profile for the absorber layer were "as-deposited", "after-degradation" and "recovery", along with the band gap of the absorber layers.

- JV and QE% as deposited.
- JV and QE% after degradation.
- JV and QE% after recovery.

The results for JV characteristics along with QE% for as-deposited samples were plotted in Figures 13 and 14. From the figures, it is visible that solar-cell structure with $MAPbI_3$ as the absorber layer has a higher PCE% than other structures, as well as QE%. The reason for this is because of good band alignment and high absorption coefficient with respect to the other two samples, whereas high open-circuit voltage was achieved for the sample $CsPbI_3$ due to its wider band gap.
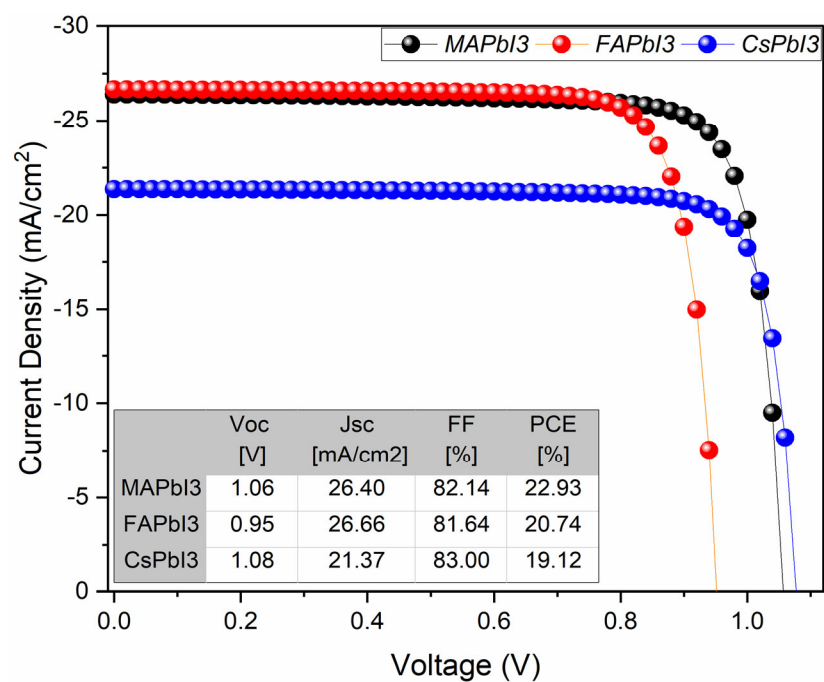
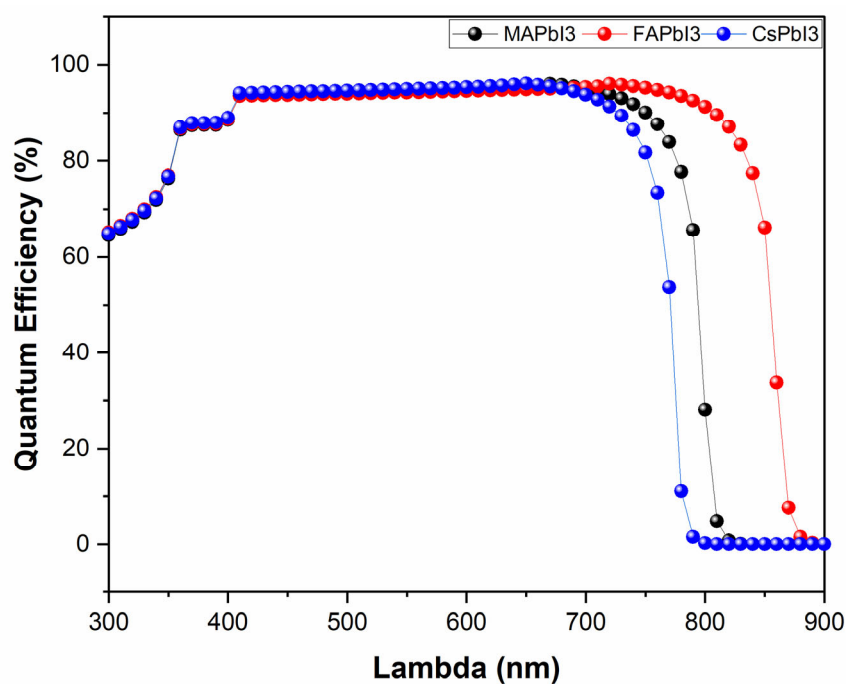**Figure 13.** J-V curve of fabricated samples; $MAPbI_3$, $FAPbI_3$, and $CsPbI_3$.



**Figure 14.** Quantum efficiency of fabricated samples; $MAPbI_3$, $FAPbI_3$, and $CsPbI_3$.

Similarly, results for JV and QE characteristics after degradation were also plotted in Figures 15 and 16 below. Figure 15 clearly shows that degradation highly affects the performance of $FAPbI_3$ by reducing its open-circuit voltage ($V_{oc}$) and short circuit current ($J_{sc}$).
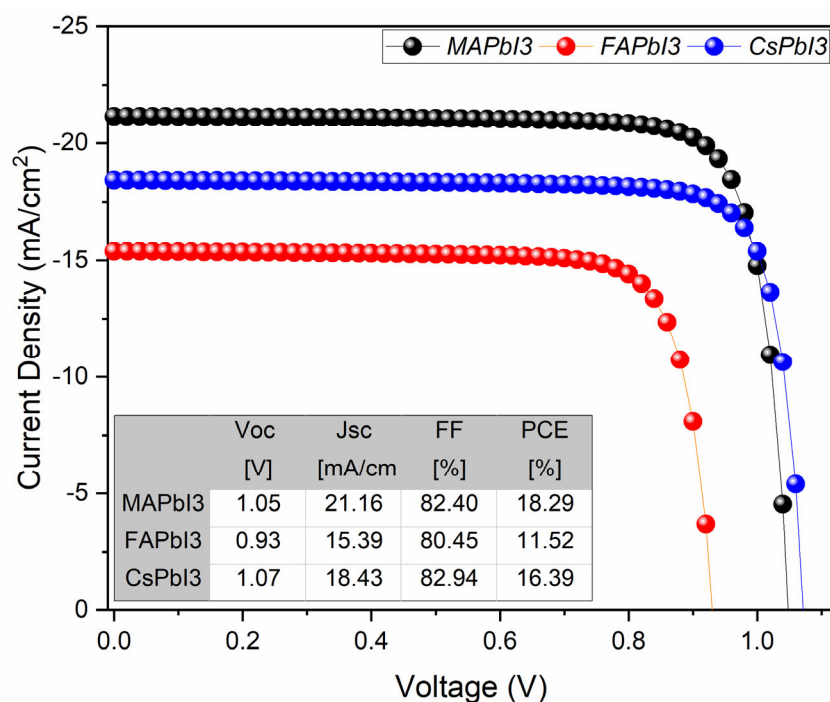
**Figure 15.** J-V curve of fabricated samples degraded; $MAPbI_3$, $FAPbI_3$, and $CsPbI_3$.

Based on these results we calculated the percentage loss of PCE in each solar cell, and for this, a formula was devised to find the percentage of loss in PCE% during the degradation of a solar cell. % loss formula is shown in Equation (3) below

$$\% \; loss = \frac{PCE_{FS} - PCE_{DS}}{|PCE_{FS}|} \times 100 \tag{3}$$

where $PCE_{FS}$ is the fabricated samples power-conversion efficiency estimated in SCAPS-1D software and $PCE_{DS}$ is the degraded samples power-conversion efficiency estimated in SCAPS-1D after degradation. Results for % loss are shown in Table 5, and it is clearly shown that $FAPbI_3$ is highly affected by degradation and $CsPbI_3$ shows more stability.
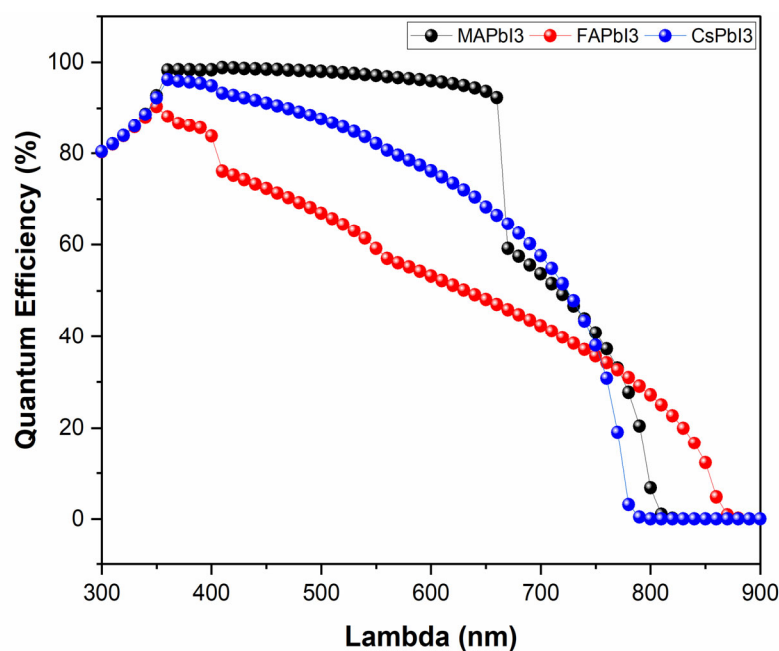


**Figure 16.** Quantum efficiency of fabricated samples degraded; $MAPbI_3$, $FAPbI_3$, and $CsPbI_3$.

Similarly, in the last section, we apply the recovery mechanism in SCAPS-1D for given solar-cell structures, and results are drawn in Figures 17 and 18.
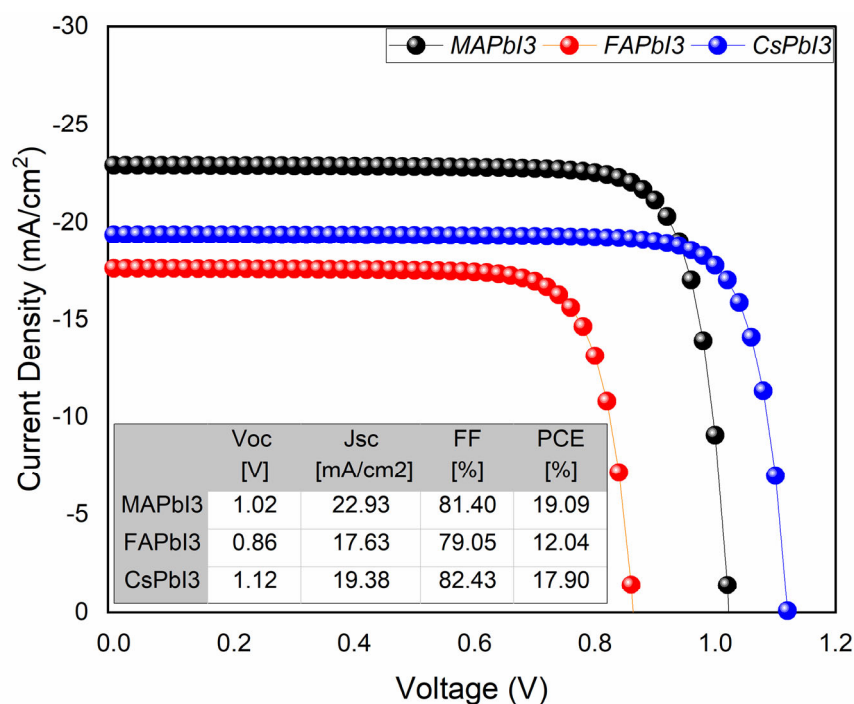


| | Voc [V] | Jsc [mA/cm2] | FF [%] | PCE [%] |
|---|---|---|---|---|
| MAPbI3 | 1.02 | 22.93 | 81.40 | 19.09 |
| FAPbI3 | 0.86 | 17.63 | 79.05 | 12.04 |
| CsPbI3 | 1.12 | 19.38 | 82.43 | 17.90 |

**Figure 17.** J-V curve of fabricated samples recovered; $MAPbI_3$, $FAPbI_3$, and $CsPbI_3$.
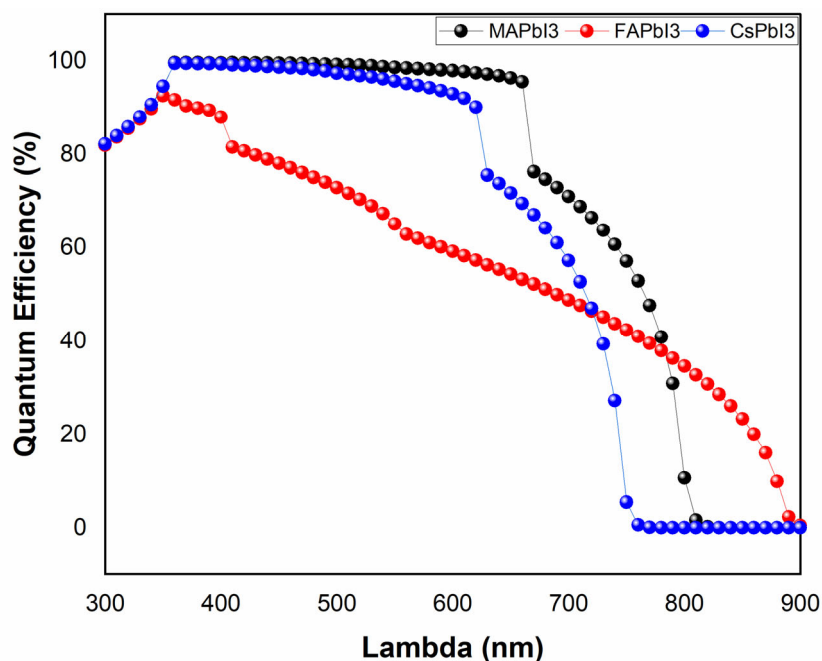


**Figure 18.** Quantum efficiency of fabricated samples recovered; $MAPbI_3$, $FAPbI_3$, and $CsPbI_3$.

Similar to % loss, a formula was also devised to find the % gain after recovery of perovskite thin films, and the formula is shown below in Equation (4).

$$\% \, gain = \frac{PCE_{RS} - PCE_{DS}}{|PCE_{DS}|} \times 100 \tag{4}$$

The results for the given formula are drawn in Table 6. Where $PCE_{RS}$ is the recovered samples power-conversion efficiency and $PCE_{DS}$ is the degraded samples power-conversion efficiency. From Table 6, it is clearly shown that $CsPbI_3$ has proven to be more stable.

**Table 6.** Percentage gain in different fabricated solar cells PCE; $MAPbI_3$, $FAPbI_3$, and $CsPbI_3$.

| Samples | Degraded Samples PCE [%] | Recovered Samples PCE [%] | Gain Percentage in PCE [%] |
|---------|--------------------------|---------------------------|----------------------------|
| $MAPbI_3$ | 18.29 | 19.09 | 4.37 |
| $FAPbI_3$ | 11.52 | 12.04 | 4.51 |
| $CsPbI_3$ | 16.39 | 17.90 | 9.21 |

## 7. Conclusions

The one-step spin-coating technique has successfully prepared $CsPbI_3$ thin films. The effect of cation A was investigated by XRD, SEM, optical analysis, and SCAPS-1D solar-cell numerical analysis software. The XRD analysis displays an extraordinary intensity of peak (110) by treating $CsPbI_3$ film with the chlorobenzene antisolvent, leading to large grains of $CsPbI_3$ thin film examined by SEM and AFM analysis. Furthermore, the enhancement of light absorption was observed more effectively. To investigate the degradation effect on device performance, a numerical analysis was performed with device structures $Spiro - OMeTAD/MAPbI_3/TiO_2$, $Spiro - OMeTAD/FAPbI_3/TiO_2$ and $Spiro - OMeTAD/CsPbI_3/TiO_2$. Based on the results presented, it was found that $CsPbI_3$ thin films are suitable candidates for efficient, stable, and durable perovskite devices.

## References

1. Lakhdar, N.; Hima, A. Electron transport material effect on performance of perovskite solar cells based on CH3NH3GeI3. *Opt. Mater.* **2019**, *99*, 109517.
2. Bouich, A.; Mari, B.; Atourki, L.; Ullah, S.; Touhami, M.E. Shedding light on the effect of diethyl ether antisolvent on the growth of (CH3NH3) PbI3 thin films. *JOM* **2021**, *73*, 551–557.
3. Rai, S.; Pandey, B.K.; Dwivedi, D.K. Modeling of highly efficient and low cost CH3NH3Pb(I1-xClx)3 based perovskite solar cell by numerical simulation. *Opt. Mater.* **2019**, *100*, 109631.
4. Khattak, Y.H.; Vega, E.; Baig, F.; Soucase, B.M. Performance investigation of experimentally fabricated lead iodide perovskite solar cell via numerical analysis. *Mater. Res. Bull.* **2022**, *151*, 111802.
5. Ma, T.; Wang, S.; Zhang, Y.; Zhang, K.; Yi, L. The development of all-inorganic CsPbX3 perovskite solar cells. *J. Mater. Sci.* **2019**, *55*, 464–479.

6. Ding, M.; Sun, L.; Chen, X.; Luo, T.; Ye, T.; Zhao, C.; Zhang, W.; Chang, H. Air-processed, large grain perovskite films with low trap density from perovskite crystal engineering for high-performance perovskite solar cells with improved ambient stability. *J. Mater. Sci.* **2019**, *54*, 12000–12011.

7. Hu, R.; Hou, W.; Han, G.; Ou, T.; Chang, Y.; Xiao, Y. Interfacial chemical bridge constructed by l-cysteine for highly efficient perovskite solar cells. *Mater. Res. Bull.* **2021**, *149*, 111698.

8. Khattak, Y.H.; Baig, F.; Shuja, A.; Beg, S.; Soucase, B.M. Numerical analysis guidelines for the design of efficient novel nip structures for perovskite solar cell. *Sol. Energy* **2020**, *207*, 579–591.

9. Kojima, A.; Teshima, K.; Shirai, Y.; Miyasaka, T. Organometal Halide Perovskites as Visible-Light Sensitizers for Photovoltaic Cells. *J. Am. Chem. Soc.* **2009**, *131*, 6050–6051.

10. Basumatary, P.; Agarwal, P. A short review on progress in perovskite solar cells. *Mater. Res. Bull.* **2022**, *149*, 111700.

11. Im, J.-H.; Lee, C.-R.; Lee, J.-W.; Park, S.-W.; Park, N.-G. 6.5% efficient perovskite quantum-dot-sensitized solar cell. *Nanoscale* **2011**, *3*, 4088–4093.

12. Kim, H.-S.; Lee, C.-R.; Im, J.-H.; Lee, K.-B.; Moehl, T.; Marchioro, A.; Moon, S.-J.; Humphry-Baker, R.; Yum, J.-H.; Moser, J.E.; et al. Lead Iodide Perovskite Sensitized All-Solid-State Submicron Thin Film Mesoscopic Solar Cell with Efficiency Exceeding 9%. *Sci. Rep.* **2012**, *2*, 591.

13. Doumbia, Y.; Bouich, A.; Soro, D.; Soucase, B.M. Mixed halide head perovskites thin films: Stability and growth investigation. *Optik* **2022**, *261*, 169222.

14. Yalçin, L.; Öztürk, R. Performance comparison of c-Si, mc-Si and a-Si thin film PV by PVsyst simulation. *J. Optoelectron. Adv. Mater.* **2013**, *15*, 326–334.

15. Devi, C.; Mehra, R. Device simulation of lead-free MASnI3 solar cell with CuSbS2 (copper antimony sulfide). *J. Mater. Sci.* **2019**, *54*, 5615–5624.

16. Stoumpos, C.C.; Malliakas, C.D.; Kanatzidis, M.G. Semiconducting Tin and Lead Iodide Perovskites with Organic Cations: Phase Transitions, High Mobilities, and Near-Infrared Photoluminescent Properties. *Inorg. Chem.* **2013**, *52*, 9019–9038.

17. Green, M.A.; Emery, K.; King, D.L.; Igari, S.; Warta, W. Solar cell efficiency tables (Version 55). *Prog. Photovoltaics Res. Appl.* **2020**, *28*, 3–15.

18. Yoshikawa, K.; Kawasaki, H.; Yoshida, W.; Irie, T.; Konishi, K.; Nakano, K.; Uto, T.; Adachi, D.; Kanematsu, M.; Uzu, H.; et al. Silicon heterojunction solar cell with interdigitated back contacts for a photoconversion efficiency over 26%. *Nat. Energy* **2017**, *2*, 17032.

19. Chowdhury, M.S.; Shahahmadi, S.; Chelvanathan, P.; Tiong, S.; Amin, N.; Techato, K.; Nuthammachot, N.; Chowdhury, T.; Suklueng, M. Effect of deep-level defect density of the absorber layer and n/i interface in perovskite solar cells by SCAPS-1D. *Results Phys.* **2020**, *16*, 102839.

20. Chen, P.; Wang, E.; Yin, X.; Xie, H.; Que, M.; Liu, J.; Gao, B.; Que, W. Highly efficient and reproducible planar perovskite solar cells with mitigated hysteresis enabled by sequential surface modification of electrodes. *J. Mater. Sci.* **2018**, *53*, 16062–16073.

21. Zhang, J.; Tan, C.H.; Du, T.; Morbidoni, M.; Lin, C.T.; Xu, S.; Durrant, J.R.; McLachlana, M.A. ZnO-PCBM bilayers as electron transport layers in low-temperature processed perovskite solar cells. *Sci. Bull.* **2018**, *63*, 343–348.

22. Raoui, Y.; Ez-Zahraouy, H.; Tahiri, N.; el Bounagui, O.; Ahmad, S.; Kazim, S. Performance analysis of MAPbI3 based perovskite solar cells employing diverse charge selective contacts: Simulation study. *Sol. Energy* **2019**, *193*, 948–955.

23. Du, Y.; Liu, P.; Li, F.; Hou, X.; Zhang, H.; Shi, Y.; Wang, S.; Wang, Y.; Guo, S.; Tai, Q.; et al. Precursor engineering for performance enhancement of hole-transport-layer-free carbon-based MAPbBr3 perovskite solar cells. *J. Alloys Compd.* **2020**, *832*, 154902.

24. Malouangou, M.D.; Yang, Y.; Zhang, Y.; Bai, L.; Matondo, J.T.; Mbumba, M.; Akram, M.W.; Guli, M. Facilitate hole transport with thin 2D perovskite capping layer to passivate interface defects of 3D perovskite solar cells using PEABr. *Mater. Res. Bull.* **2022**, *150*, 111793.

25. Mohammed, M.K.A.; Sarusi, G.; Sakthivel, P.; Ravi, G.; Younis, U. Improved stability of ambient air-processed methylammonium lead iodide using carbon nanotubes for perovskite solar cells. *Mater. Res. Bull.* **2021**, *137*, 111182.

26. Pitchaiya, S.; Natarajan, M.; Santhanam, A.; Asokan, V.; Ramakrishnan, V.M.; Selvaraj, Y.; Yuvapragasam, A.; Rangasamy, B.; Sundaram, S.; Velauthapillai, D. The Performance of CH3NH3PbI3—Nanoparticles based—Perovskite Solar Cells Fabricated by Facile Powder press Technique. *Mater. Res. Bull.* **2018**, *108*, 61–72.

27. Bouich, A.; Ullah, S.; Marí, B.; Atourki, L.; Touhami, M.E. One-step synthesis of FA1-xGAxPbI3 perovskites thin film with enhanced stability of alpha (α) phase. *Mater. Chem. Phys.* **2020**, *258*, 123973.

28. Fradi, K.; Bouich, A.; Slimi, B.; Chtourou, R. Towards improving the optoelectronics properties of MAPbI3(1−x)B3x/ZnO heterojunction by bromine doping. *Optik* **2022**, *249*, 168283.

29. Azri, F.; Meftah, A.A.; Sengouga, N.; Meftah, A.A. Electron and hole transport layers optimization by numerical simulation of a perovskite solar cell. *Sol. Energy* **2019**, *181*, 372–378.

30. Watthage, S.C.; Song, Z.; Phillips, A.B.; Heben, M.J. *Evolution of Perovskite Solar Cells, in Perovskite Photovoltaics*; Elsevier: Amsterdam, The Netherlands, 2018; pp. 43–88.

31. Shang, Q.; Li, M.; Zhao, L.; Chen, D.; Zhang, S.; Chen, S.; Gao, P.; Shen, C.; Xing, J.; Xing, G.; et al. Role of the Exciton–Polariton in a Continuous-Wave Optically Pumped CsPbBr 3 Perovskite Laser. *Nano Lett.* **2020**, *20*, 6636–6643.

**32.** Saliba, M.; Wood, S.M.; Patel, J.B.; Nayak, P.K.; Huang, J.; Alexander-Webber, J.A.; Wenger, B.; Stranks, S.D.; Hörantner, M.T.; Wang, J.T.-W.; et al. Structured Organic-Inorganic Perovskite toward a Distributed Feedback Laser. *Adv. Mater.* **2016**, *28*, 923–929.

33.  Zhou, N.; Bekenstein, Y.; Eisler, C.N.; Zhang, D.; Schwartzberg, A.M.; Yang, P.; Alivisatos, A.P.; Lewis, J.A. Perovskite nanowire–block copolymer composites with digitally programmable polarization anisotropy. *Sci. Adv.* **2019**, *5*, eaav8141.
34.  Lin, K.; Xing, J.; Quan, L.N.; De Arquer, F.P.G.; Gong, X.; Lu, J.; Xie, L.; Zhao, W.; Zhang, D.; Yan, C.; et al. Perovskite light-emitting diodes with external quantum efficiency exceeding 20 per cent. *Nature* **2018**, *562*, 245–248.
35.  Xiao, Z.; Kerner, R.A.; Zhao, L.; Tran, N.L.; Lee, K.M.; Koh, T.-W.; Scholes, G.D.; Rand, B.P. Efficient perovskite light-emitting diodes featuring nanometre-sized crystallites. *Nat. Photonics* **2017**, *11*, 108–115.
36.  Lee, Y. et al., High-Performance Perovskite-Graphene Hybrid Photodetector, Adv. Mater., vol. 27, no. 1, pp. 41–46, Jan. 2015.
37.  Hu, X.; Zhang, X.; Liang, L.; Bao, J.; Li, S.; Yang, W.; Xie, Y. High-Performance Flexible Broadband Photodetector Based on Organolead Halide Perovskite. *Adv. Funct. Mater.* **2014**, *24*, 7373–7380.
38.  Wu, T.; Qin, Z.; Wang, Y.; Wu, Y.; Chen, W.; Zhang, S.; Cai, M.; Dai, S.; Zhang, J.; Liu, J.; et al. The Main Progress of Perovskite Solar Cells in 2020–2021. *Nano-Micro Lett.* **2021**, *13*, 1–18.
39.  Akman, E.; Shalan, A.E.; Sadegh, F.; Akin, S. Moisture-Resistant FAPbI 3 Perovskite Solar Cell with 22.25 % Power Conversion Efficiency through Pentafluorobenzyl Phosphonic Acid Passivation. *ChemSusChem* **2021**, *14*, 1176–1183.
40.  Targhi, F.F.; Jalili, Y.S.; Kanjouri, F. MAPbI3 and FAPbI3 perovskites as solar cells: Case study on structural, electrical and optical properties. *Results Phys.* **2018**, *10*, 616–627.
41.  Li, X.; Wu, J.; Wang, S.; Qi, Y. Progress of All-inorganic Cesium Lead-free Perovskite Solar Cells. *Chem. Lett.* **2019**, *48*, 989–1005.
42.  Piveteau, L.; Aebli, M.; Yazdani, N.; Millen, M.; Korosec, L.; Krieg, F.; Benin, B.M.; Morad, V.; Piveteau, C.; Shiroka, T.; et al. Bulk and Nanocrystalline Cesium Lead-Halide Perovskites as Seen by Halide Magnetic Resonance. *ACS Central Sci.* **2020**, *6*, 1138–1149.
43.  Niu, Q.; Deng, Y.; Cui, D.; Lv, H.; Duan, X.; Li, Z.; Liu, Z.; Zeng, W.; Xia, R.; Tan, W.; et al. Enhancing the performance of perovskite solar cells via interface modification. *J. Mater. Sci.* **2019**, *54*, 14134–14142.
44.  Kearney, K.; Seo, G.; Matsushima, T.; Adachi, C.; Ertekin, E.; Rockett, A. Computational Analysis of the Interplay between Deep Level Traps and Perovskite Solar Cell Efficiency. *J. Am. Chem. Soc.* **2018**, *140*, 15655–15660.
45.  Zhang, L.; Lin, S. Cosensitization-based halide perovskite in aqueous solution: A photoelectrochemical and first-principles investigation. *Mater. Res. Bull.* **2021**, *141*, 111358.
46.  Rahul, P.; Singh, K.; Singh, R.; Singh, V.; Bhattacharya, B.; Khan, Z.H. New class of lead free perovskite material for low-cost solar cell application. *Mater. Res. Bull.* **2017**, *97*, 572–577.
47.  Kim, G.-H.; Kim, D.S. Development of perovskite solar cells with >25% conversion efficiency. *Joule* **2021**, *5*, 1033–1035.
48.  Bouich, A.; Hartiti, B.; Ullah, S.; Ullah, H.; Touhami, M.E.; Santos DM, F.; Mari, B. Experimental, theoretical, and numerical simulation of the performance of CuInxGa (1-x) S2-based solar cells. *Optik* **2019**, *183*, 137–147.
49.  Ma, R.; Yan, C.; Yu, J.; Liu, T.; Liu, H.; Li, Y.; Chen, J.; Luo, Z.; Tang, B.; Lu, X.; et al. High-Efficiency Ternary Organic Solar Cells with a Good Figure-of-Merit Enabled by Two Low-Cost Donor Polymers. *ACS Energy Lett.* **2022**, *7*, 2547–2556.
50.  Soucase, B.M.; Baig, F.; Khattak, Y.H.; Vega, E.; Mollar, M. Numerical analysis for efficiency limits of experimental perovskite solar cell. *Sol. Energy* **2022**, *235*, 200–208.
51.  Lin, L.; Jiang, L.; Li, P.; Xiong, H.; Kang, Z.; Fan, B.; Qiu, Y. Simulated development and optimized performance of CsPbI3 based all-inorganic perovskite solar cells. *Sol. Energy* **2020**, *198*, 454–460.
52.  Karthick, S.; Velumani, S.; Bouclé, J. Experimental and SCAPS simulated formamidinium perovskite solar cells: A comparison of device performance. *Sol. Energy* **2020**, *205*, 349–357.
53.  Shafi, M.A.; Bouich, A.; Fradi, K.; Guaita, J.M.; Khan, L.; Mari, B. Effect of deposition cycles on the properties of ZnO thin films deposited by spin coating method for CZTS-based solar cells. *Optik* **2022**, *258*, 168854.
54.  Baig, F.; Khattak, Y.H.; Beg, S.; Soucase, B.M. Numerical analysis of a novel CNT/Cu2O/Sb2Se3/In2S3/ITO antimony selenide solar cell. *Optik* **2019**, *197*, 163107.
55.  Ahn, N.; Kwak, K.; Jang, M.S.; Yoon, H.; Lee, B.Y.; Lee, J.-K.; Pikhitsa, P.V.; Byun, J.; Choi, M. Trapped charge-driven degradation of perovskite solar cells. *Nat. Commun.* **2016**, *7*, 13422.
56.  Jeong, K.; Byeon, J.; Jang, J.; Ahn, N.; Choi, M. Pulsatile therapy for perovskite solar cells. *Joule* **2022**, *6*, 1087–1102.
57.  Bouich, A.; Marí-Guaita, J.; Sahraoui, B.; Palacios, P.; Marí, B. Tetrabutylammonium (TBA)-Doped Methylammonium Lead Iodide: High Quality and Stable Perovskite Thin Films. *Front. Energy Res.* **2022**, *10*, 840817.
58.  Baig, F.; Khattak, Y.H.; Shuja, A.; Riaz, K.; Soucase, B.M. Performance investigation of Sb2Se3 based solar cell by device optimization, band offset engineering and Hole Transport Layer in SCAPS-1D. *Curr. Appl. Phys.* **2020**, *20*, 973–981.
59.  Hu, E.T.; Yue, G.Q.; Zhang, R.J.; Zheng, Y.X.; Chen, L.Y.; Wang, S.Y. Numerical simulations of multilevel impurity photovoltaic effect in the sulfur doped crystalline silicon. *Renew. Energy* **2015**, *77*, 442–446.
60.  Marí-Guaita, J.; Bouich, A.; Marí, B. Stability Improvement of Methylammonium Lead Iodide Perovskite Thin Films by Bismuth Doping. *JOM* **2022**, *74*, 3103–3110.
61.  Khattak, Y.H.; Baig, F.; Soucase, B.M.; Beg, S. Efficiency Enhancement of Cu2BaSnS4 Thin Film Solar Cell. *Mater. Focus* **2018**, *7*, 758–765.
62.  Baig, F.; Khattak, Y.H.; Soucase, B.M.; Beg, S.; Gillani, S.R.; Ahmed, S. A Baseline for the Numerical Study of Sb 2 Se 3 Absorber Material Based Solar Cell. *J. Nanoelectron. Optoelectron.* **2019**, *14*, 72–79.
63.  Jamil, M.; Ali, A.; Mahmood, K.; Arshad, M.I.; Tahir, S.; Nabi, M.A.U.; Ikram, S.; Amin, N.; Hussain, S. Numerical simulation of perovskite/Cu2Zn(Sn1-x Gex)S4 interface to enhance the efficiency by valence band offset engineering. *J. Alloys Compd.* **2019**, *821*, 153221.

64. Bouich, A.; Marí-Guaita, J.; Bouich, A.; Pradas, I.G.; Marí, B. Towards manufacture stable lead perovskite APbI3 (A= Cs, MA, FA) based solar cells with low-cost techniques. *Eng. Proc.* **2022**, *12*, 81.

65. Khattak, Y.H.; Baig, F.; Marí, B.; Beg, S.; Ahmed, S. Baseline for the Numerical Analysis of High Efficiency Copper Manganese Tin Sulfide Cu 2 MnSnS 4 Based Thin Film Solar Cell. *J. Nanoelectron. Optoelectron.* **2018**, *13*, 1678–1684.

66. Bouazizi, S.; Tlili, W.; Bouich, A.; Mari, B.; Omri, A. Design and efficiency enhancement of FTO/PC60BM/CsSn0. 5Ge0. 5I3/Spiro-OMeTAD/Au perovskite solar cell utilizing SCAPS-1D Simulator. *Mater. Res. Express* **2022**.

67. Marí-Guaita, J.; Bouich, A.; Marí, B. Shedding Light on Phase Stability and Surface Engineering of Formamidinium Lead Iodide (FaPbI3) Thin Films for Solar Cells. *Eng. Proc.* **2021**, *12*, 1.

68. Bouich, A.; Marí-Guaita, J.; Soucase, B.M.; Palacios, P. Manufacture of High-Efficiency and Stable Lead-Free Solar Cells through Antisolvent Quenching Engineering. *Nanomaterials* **2022**, *12*, 2901.

69. Shafi, M. A.; Khan, L.; Ullah, S.; Shafi, M. Y.; Bouich, A.; Ullah, H.; Mari, B. Novel compositional engineering for~ 26% efficient CZTS-perovskite tandem solar cell. *Optik* **2022**, *253*, 168568.

70. Marí-Guaita, J.; Bouich, A.; Shafi, M. A.; Bouich, A.; Marí, B. Investigation on the stability and efficiency of MAPbI3 and MASnI3 thin films for Solar Cells. *Phys. Status Solidi (A)* **2022**, *219*, 2100664.

71. Bouich, A. Study and Characterization of Hybrid Perovskites and Copper-Indium-Gallium Selenide Thin Films for Tandem Solar cells. Doctoral dissertation, Universitat Politècnica de València, Valencia, Spain, 2021.

72. Soro, D.; Sylla, A.; Toure, A.; Bouich, A.; Toure, S.; Marí, B. Simulation of a CIGS Solar Cell with CIGSe2/MoSe2/Mo Rear Contact Using AFORS-HET Digital Simulation Software. *Modeling Numer. Simul. Mater. Sci.* **2022**, *12*, 13–23.

73. Tarbi, A.; Chtouki, T.; Bouich, A.; Elkouari, Y.; Erguig, H.; Migalska-Zalas, A.; Aissat, A. InP/InGaAsP thin films based solar cells: Lattice mismatch impact on efficiency. *Opt. Mater.* **2022**, *131*, 112704.